Ocean Engineering 238 (2021) 109730

Contents lists available at ScienceDirect

Ocean Engineering

journal homepage: www.elsevier.com/locate/oceaneng

Numerical study of vortex-induced vibration of a flexible cylinder with large aspect ratios in oscillatory flows

Di Deng [a], Weiwen Zhao [a], Decheng Wan [a,b,*]

[a] Computational Marine Hydrodynamics Lab (CMHL), School of Naval Architecture, Ocean and Civil Engineering, Shanghai Jiao Tong University, Shanghai, 200240, China

[b] Ocean College, Zhejiang University, Zhoushan, 316021, China

ARTICLE INFO

Keywords:
Vortex-induced vibration
viv-FOAM-SJTU solver
Oscillatory flow
Aspect ratio

ABSTRACT

Numerical investigations on vortex-induced vibration (VIV) of a flexible cylinder with different length to diameter ratios, named the aspect ratio (L/D), ranging from 167 to 667 in an oscillatory flow have been conducted by the viv-FOAM-SJTU solver. The solver is developed based on the open source toolbox OpenFOAM and the two-dimensional (2D) strip theory. Hydrodynamic forces are calculated through the PIMPLE algorithm in each 2D fluid strip. The Finite Element Method (FEM) combined with the Newmark-β method are used to calculate vibrations of the flexible cylinder in both crossflow and inline directions. The cylinder model is pinned at both ends with top and bottom support frames forced to harmonically oscillate in the inline direction, which contributes to the generation of a relative oscillatory flow between the still water and the flexible cylinder. Mesh and fluid strip convergence studies are conducted to choose the appropriate computational model for subsequent simulations. Simulation results and experiment results are in good agreement that verifies the validity of the solver. Comparisons among simulations with different aspect ratios are analyzed detailedly. The maximum vibration amplitude, the dominant vibration mode and the non-dimensional dominant vibration frequency in both directions are enlarged apparently with the increase of the cylinder aspect ratio. The typical vibration trajectory changes from the butterfly type to the stripe type with L/D increases.

1. Introduction

When the viscous flow with a certain velocity goes through a circular cylinder, vortices will be generated on the cylinder surface and then shed behind the cylinder. The asymmetric vortex shedding contributes to the fluctuated lift force in the cross-flow direction, which then leads to the VIV phenomenon. When the vortex shedding frequency approaches around the cylinder natural frequency, the resonance phenomenon happens and the vibration amplitude will be amplified obviously. In deep sea oil and gas exploitation, VIV of the marine riser is one of the main sources resulting in the fatigue damage. During the past decades, VIV features of a single cylinder had been studied extensively by researchers, such as Williamson and Govardhan (2004), Sarpkaya (2004), Huang et al. (2009), Ji et al. (2015), Chen et al. (2016) and Wan and Duan (2017). In order to predict VIV response of the deep sea riser, the 2D strip method was proposed by Willden and Graham (2001, 2004) and benchmark simulations were conducted to verify its validity. Meanwhile, the multi-modes vibration phenomenon was observed when the cylinder aspect ratio was extremely large. Yamamoto et al. (2004) and Sun et al. (2012) also adopted this method to carry out VIV researches. Simulation results were in good agreement with published data and experiment results, which further verified the validity of the strip method.

Researches on VIV of a flexible cylinder in the oscillatory flow are comparatively fewer than that in the steady flows. The relative oscillatory flow is generated between the marine riser and the water due to the periodical top end oscillation of the riser connected to the floating platform, which results from the effects of winds, waves and currents in the ocean environment. The complexity of the oscillatory flow leads to different VIV responses of the cylinder from that in the steady flow. Therefore, VIV of a rigid cylinder in oscillatory flow was studied firstly to capture its vibration and vortex shedding features. Williamson (1985) and Sarpkaya (1986) conducted experiments on VIV of a rigid cylinder in the relative oscillatory flow systematically and representative vortex

* Corresponding author. Computational Marine Hydrodynamics Lab (CMHL), School of Naval Architecture, Ocean and Civil Engineering, Shanghai Jiao Tong University, Shanghai, 200240, China.

E-mail address: dcwan@sjtu.edu.cn (D. Wan).

https://doi.org/10.1016/j.oceaneng.2021.109730
Received 10 April 2021; Received in revised form 23 July 2021; Accepted 21 August 2021
Available online 30 August 2021

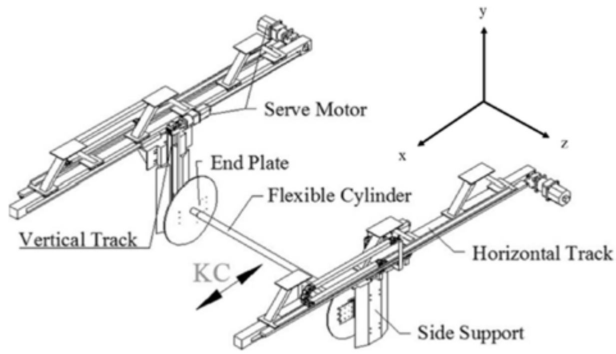

Fig. 1. Layout of the model experiments (Fu et al., 2013).

Table 1
Main parameters of the flexible cylinder.

	Symbols	Values	Units
Mass ratio	m^*	1.53	-
Diameter	D	0.024	m
Length	L	4	m
Bending stiffness	EI	10.5	Nm^2
Top tension	T_t	500	N
The first natural frequency	f_n^1	2.68	Hz
The second natural frequency	f_n^2	5.46	Hz
Keulegan-Carpenter number	KC	178	-

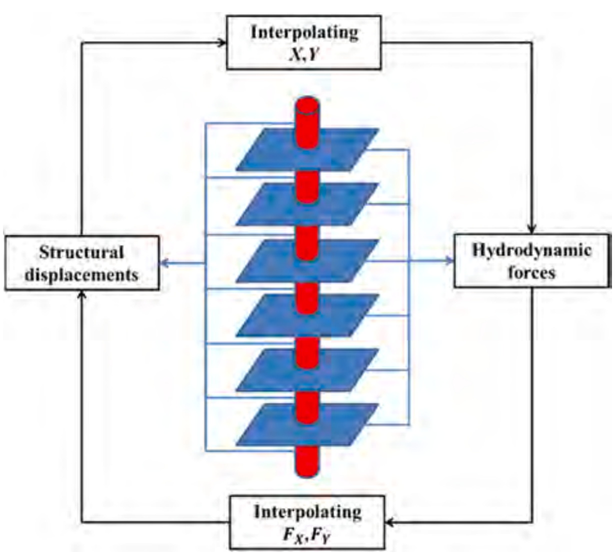

Fig. 2. The schematic diagram of the 2D strip method.

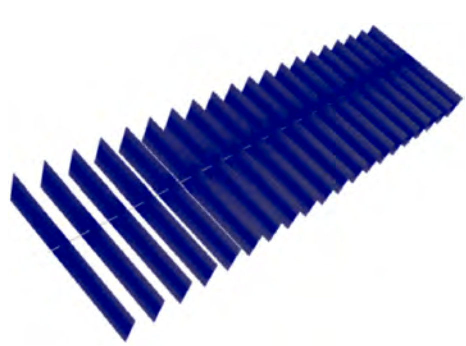

Fig. 3. Layout of the computational model.

shedding regimes were identified within a particular range of Keulegan-Carpenter (*KC*) Numbers. Bearman (1989) studied the effects of *KC* numbers and Stokes numbers through the experimental method, while different vortex shedding regimes were observed too. In order to deeply understand the vibration responses, Sumer and Fredsøe (1988) carried out experiments on transverse vibration of a rigid cylinder exposed to the oscillatory flow with *KC* numbers ranging from 5 to 100. Kozakiewicz et al. (1997) and Zhao et al. (2012) carried out experiments and numerical simulations on VIV of a fixed and a freely vibrating circular cylinder in relative oscillatory flow with different reduced velocities at $KC = 10$ and 20 respectively. They found that the vortex shedding direction and wake structures changed apparently due to the crossflow vibration of the cylinder. Zhao et al. (2012) also concluded that the reduced velocity presented significant effects on the XY-trajectory mode of the cylinder. And the maximum crossflow vibration amplitude was comparatively smaller than that in the inline direction when the reduced velocity was extremely large. Further, Zhao et al. (2013a, 2013b) carried out simulations on VIV of a cylinder with one-DoF (Degree of Freedom) and two-DoFs experiencing the oscillatory flow and the mixed flow respectively.

Nehari et al. (2004) concentrated on the numerical method effects to VIV response of a circular cylinder between three-dimensional (3D) and two-dimensional (2D) models. Scandura et al. (2009) investigated vorticity dynamics and forces induced by the oscillatory flow over a circular cylinder adopting the Direct Numerical Simulation (DNS) method. Zhao and Cheng (2014) also conducted researches on vortex shedding regimes of two circular cylinders in tandem and side-by-side arrangements using 2D model. Effects of *KC* numbers and gap ratios between two cylinders were mainly investigated. Tong et al. (2015) focused on flow patterns of four cylinders in square arrangement exposed to the oscillatory flow under low *KC* numbers and Reynolds (*Re*) numbers. Flow patterns were classified based on the known flow regimes around a single cylinder. Pearcey et al. (2017) performed 2D investigations on transverse vibration of two rigid connected cylinders with different diameter at $KC = 10$. Orientation and gap effects were mainly studied varying from the tandem arrangement to the side-by-side arrangement. The specific intermittent switch among different vortex regimes was observed. Munir et al. (2018) carried out 2D numerical simulations considering the plane boundary effects. Simulations were conducted at $KC = 5$ and 10 with the reduced velocities varied from 1 to 15, while four gap ratios between the cylinder and the plane were mainly investigated. It was found that the plane boundary played significant effects in the crossflow vibration response of the cylinder. Non-vortex shedding regime was observed at large reduced velocity at $KC = 10$ resulting from absorption effects of shear layers generated from the plane boundary to vortices. Meanwhile, Fonias and Grigoriadis (2018) also carried out similar researches using the 3D simulation model. They found that the suppression of the boundary layer separation phenomenon would happen when the gap ratio was smaller than 0.05.

Nevertheless, VIV of a long flexible cylinder showed quite different vibration characteristics resulting from the axial deformation. Fu et al. (2013) and Wang et al. (2014) carried out experiments on VIV of a flexible cylinder in the oscillatory flow at $KC = 178$ and 84 respectively. The specific "Building up – Lock in – Dying out" VIV developing process was proposed. Effects of the oscillating period on VIV features were studied. Furthermore, Wang et al. (2015) studied the fatigue damage induced by VIV in the oscillatory flow adopting an empirical VIV predicting model. Thorsen et al. (2016) and Yuan et al. (2018) also proposed semi-empirical models to predict VIV response in the oscillatory flow. Based on experiments of Wang et al. (2014), Fu et al. (2018) carried out numerical simulations at the same condition and compared with experiment results detailedly. Ren et al. (2019) carried out experiments on VIV of a flexible cylinder fitted with helical strakes in the oscillatory flow with *KC* numbers varying from 21 to 165. Effects on VIV suppression features from the helical strakes are mainly studied. However, most previous researches mainly concentrated on comparatively

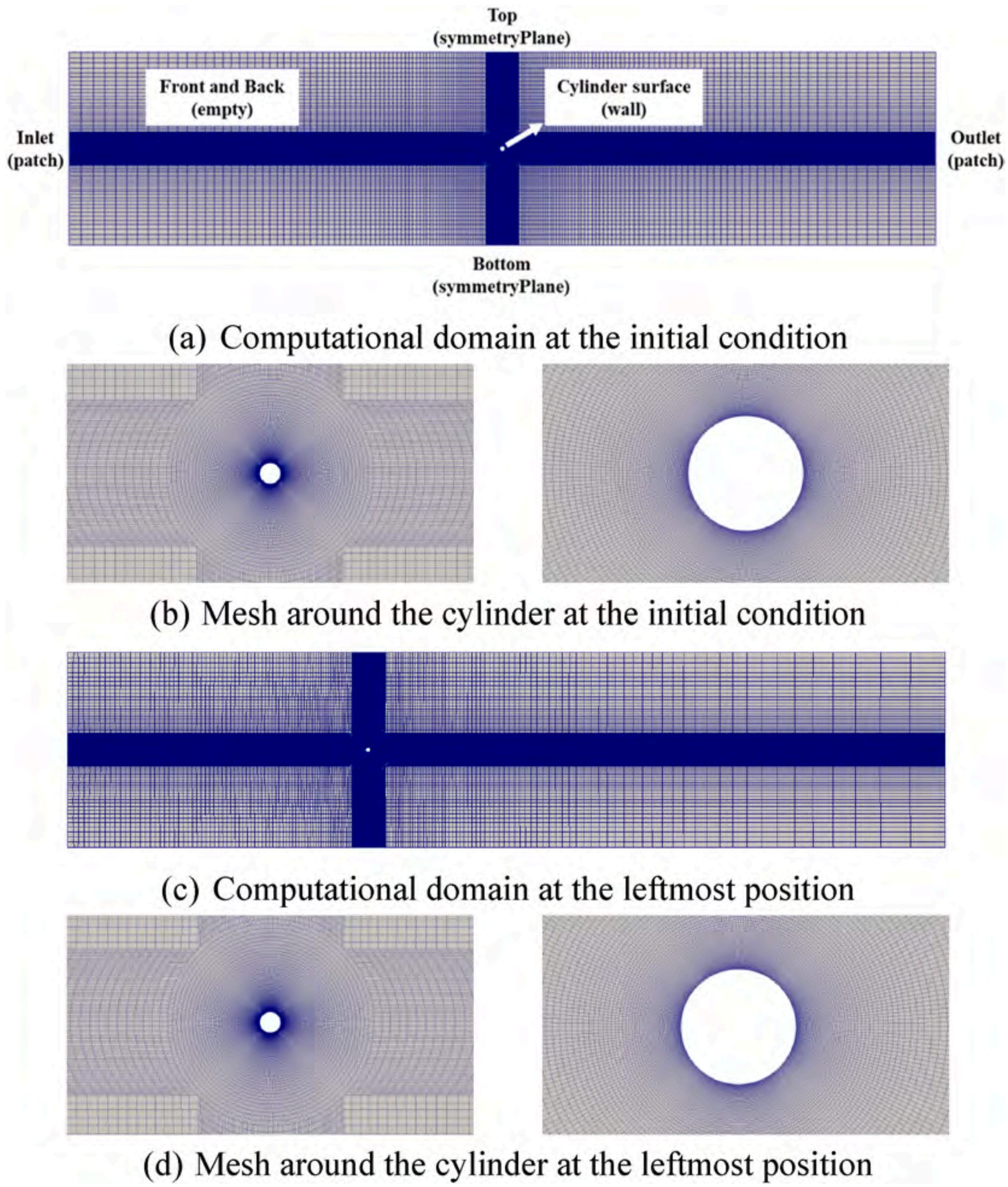

Fig. 4. Computational domain and mesh around the cylinder surface of each fluid strip.

low aspect ratio, which was smaller than 200. Actually, VIV of a flexible cylinder with large aspect ratio shows more complicated characteristics, such as extreme high vibration mode, the travelling wave phenomenon, multi-modes vibration and etc. Lie and Kaasen (2006) carried out experiments of a large-scale cylinder in the sheared flow with the aspect ratio reached 3000. The maximum 29th vibration mode and the obvious travelling wave phenomenon along the cylinder span were observed. Xu et al. (2008) adopted the wake oscillator model to study VIV of a flexible cylinder with high aspect ratio in uniform and sheared flows. They found that nonlinear effects become more significant with the increase of the cylinder aspect ratio. Duan et al. (2017) also studied VIV responses in uniform and sheared flow conditions with the cylinder aspect ratio ranging from 500 to 1000. They found that the multi-modes vibration phenomenon become more obvious especially at high aspect ratios.

Although abundant researches of a large-scale flexible cylinder in steady flow conditions had been conducted using both experimental and numerical methods, studies on VIV in the oscillatory flow with similar cylinder model were limited. Hence, effects of the cylinder aspect ratio to VIV responses in the oscillatory flow are mainly studied in this paper using the viv-FOAM-SJTU solver based on experiments of Fu et al. (2013) and simulations of Fu et al. (2018). The cylinder aspect ratio varies from 167 to 667. Particular variations on the mode transition phenomenon in the half oscillatory period and vibration trajectories along the cylinder are analyzed. This paper is organized as followed: the numerical method used in this paper is introduced in Section 2, followed by validation studies in section 3, including the mesh convergence study, the fluid strip number convergence study and the verification study of the solver. Simulation results and corresponding discussions are presented in section 4. Finally, Section 5 gives a brief summary.

2. Numerical method

2.1. Problem description

In this paper, the fundamental simulation is carried out referring to

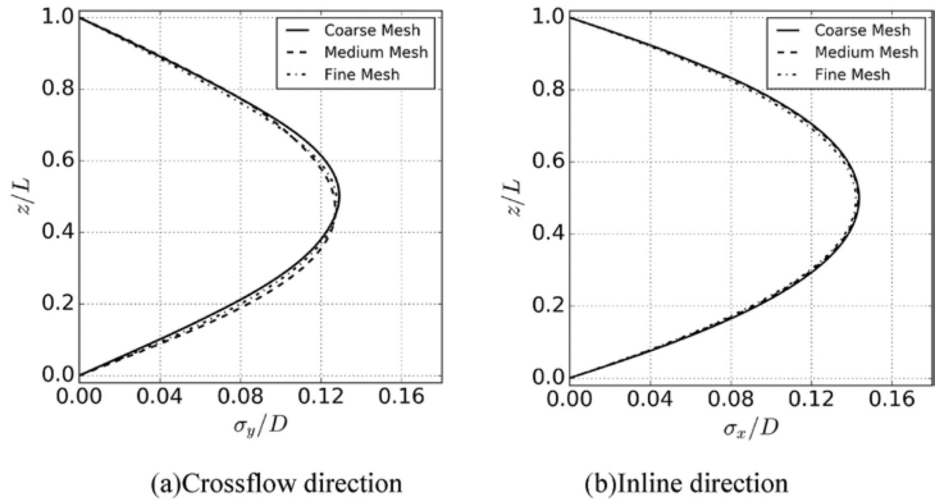

Fig. 5. Comparison of non-dimensional vibration displacement STD of the cylinder among different mesh resolutions in both directions.

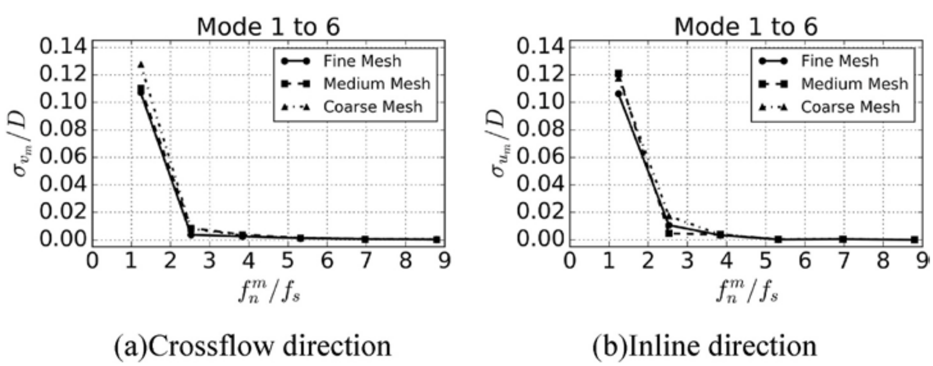

Fig. 6. Comparison of non-dimensional vibration modal weights STD of the cylinder among different mesh resolutions in both directions.

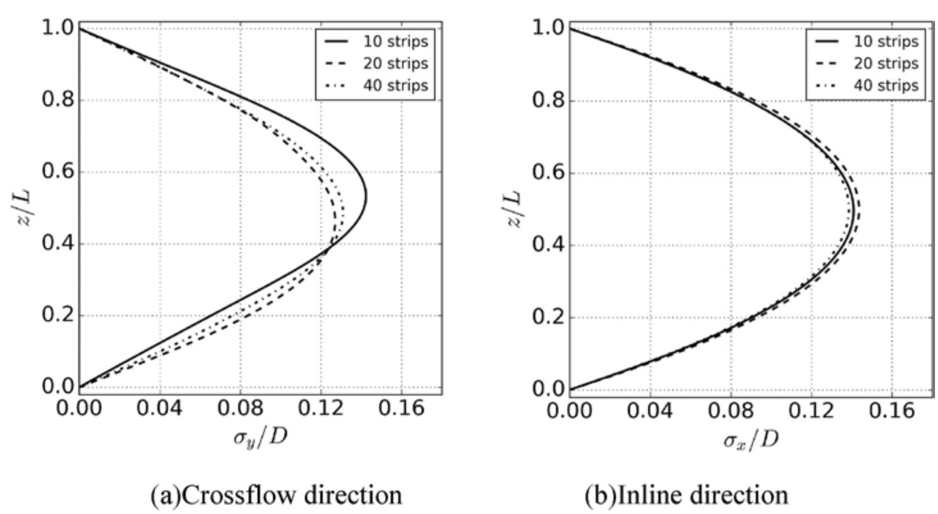

Fig. 7. Comparison of non-dimensional vibration displacement STD of the cylinder among different number of fluid strips in both directions.

experiments of Fu et al. (2013). The layout of model experiments is shown in Fig. 1. The water keeps still and support frames at both ends of the horizontal flexible cylinder are forced to oscillate in the inline direction (x direction), while the cylinder is allowed to freely vibrate in the crossflow direction (y direction). Main parameters of the cylinder model are listed in Table 1. The periodical oscillation of support frames can be expressed as Eq (1) and Eq (2):

$$A(t) = A_m \cdot \sin\left(\frac{2\pi}{T} t\right) \quad (1)$$

$$U(t) = \frac{2\pi \cdot A_m}{T} \cdot \cos\left(\frac{2\pi}{T} t\right) = U_m \cdot \cos\left(\frac{2\pi}{T} t\right) \quad (2)$$

where A is the oscillating amplitude at time t; A_m is the maximum

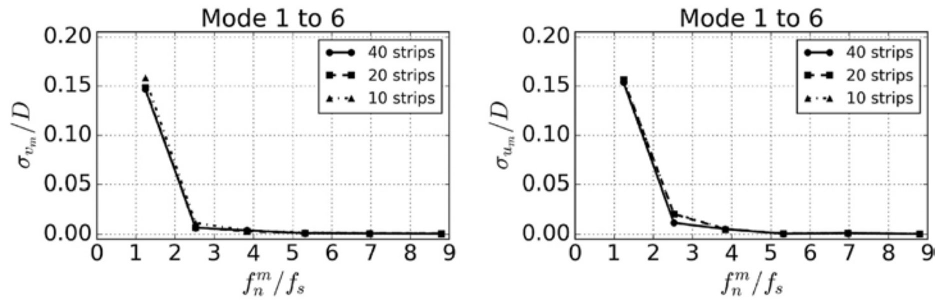

(a)Crossflow direction (b)Inline direction

Fig. 8. Comparison of non-dimensional vibration modal weights STD of the cylinder among different number of fluid strips in both directions.

oscillating amplitude; T is the oscillating period; U is the oscillating velocity at time t;U_m is the maximum oscillating velocity of support frames.

The relative oscillatory flow between the still water and the oscillating cylinder can be represented by the KC number, which denotes the connection between the maximum oscillating amplitude and the diameter of the flexible cylinder as shown in Eq (3):

$$KC = \frac{2\pi \cdot A_m}{D} \tag{3}$$

where D is the diameter of the cylinder.

2.2. Two-dimensional strip theory

For a flexible cylinder with large aspect ratio, the direct numerical simulation of the 3D fluid field will cost super-abundant computational resources and time. In order to solve this problem, Willden and Graham (2001, 2004) put forward the 2D strip method in predicting VIV responses of long flexible cylinders. This method simplifies the 3D fluid field into several 2D fluid strips equally distributed along the cylinder span. Hydrodynamic forces are calculated in each 2D strip, which then are applied to structural elements. After the computation of vibrations, nodal displacements are interpolated to the corresponding fluid strips to update the dynamic mesh and then start the next cycle of computation. The schematic diagram of the 2D strip method is shown in Fig. 2. This method is very appropriate for solving Fluid and Structure Interaction (FSI) problems with supramaximal computation domain. It owns high computational efficiency and the computational accuracy is reliable comparing with DNS method, which has been verified through previous researches, such as Meneghini et al. (2004) and Yamamoto et al. (2004).

In present study, all simulations are carried out using the viv-FOAM-SJTU solver, which is developed based on the open source toolbox OpenFOAM and the 2D strip method. Hydrodynamic forces acted on the cylinder are computed from viscous forces and pressure forces using the PIMPLE algorithm in the OpenFOAM, integrated over the surface of the cylinder in each fluid strip. The connection among all fluid strips is achieved through the inline and crossflow vibrations of the cylinder calculated from the structural field using the FEM method with the Newmark-β algorithm. The reliability of the solver in predicting VIV responses in steady flows has been verified by Duan et al. (2016a) where the benchmark simulation results have been compared with the experiment results in detail. Employing this solver, Duan et al. (2016b, 2018) and Wang et al. (2019) have conducted abundant numerical investigations on VIV of a single flexible cylinder in uniform, sheared and stepped flows respectively.

2.3. Hydrodynamic governing equations

In order to obtain VIV responses, hydrodynamic forces in both directions should be calculated first. During the simulation, the flow field is supposed to be incompressible with constant dynamic viscosity μ and constant density ρ. Reynolds-averaged Navier-Stokes equations (RANS) are chosen as hydrodynamic governing equations expressed in Eq (4) and Eq (5). The SST k-ω turbulence model is used to compute the Reynolds stress and no wall functions are used in present study. Fu et al. (2018) and Zhao (2013) also adopted the same numerical methods to investigate VIV responses of a flexible and a circular cylinder experiencing an oscillatory flow respectively and verified its reliability.

$$\frac{\partial \overline{u}_i}{\partial x_i} = 0 \tag{4}$$

$$\frac{\partial}{\partial t}\left(\rho \overline{u}_i\right) + \frac{\partial}{\partial x_j}\left(\rho \overline{u}_i \overline{u}_j\right) = -\frac{\partial \overline{p}}{\partial x_i} + \frac{\partial}{\partial x_j}\left(2\mu \overline{S}_{ij} - \rho \overline{u_j' u_i'}\right) \tag{5}$$

where $\overline{S}_{ij} = \frac{1}{2}\left(\frac{\partial \overline{u}_i}{\partial x_j} + \frac{\partial \overline{u}_j}{\partial x_i}\right)$ is the mean rate of the strain tensor; $-\rho\overline{u_j' u_i'}$ refers as the Reynolds stress τ_{ij} computed by $\tau_{ij} = -\rho\overline{u_j' u_i'} = 2\mu_t \overline{S}_{ij} - \frac{2}{3}\rho k \delta_{ij}$, where$\mu_t$is the turbulent viscosity and$k = (1/2)\overline{u_i' u_i'}$is the turbulent energy calculated from the fluctuating velocity field; δ_{ij} is the Kronecke's function.

The SST k-ω turbulence model put forward by Menter (1993) consists of the turbulence kinetic energy k and the turbulence dissipation rate ω. Transport equations of k and ω can be written as Eq (6) and Eq (7):

$$\frac{\partial(\rho k)}{\partial t} = \tau_{ij}\frac{\partial u_i}{\partial x_j} - \beta^* \rho \omega k + \frac{\partial}{\partial x_j}\left[(\mu + \sigma_k \mu_t)\frac{\partial k}{\partial x_j}\right] \tag{6}$$

$$\frac{\partial(\rho \omega)}{\partial t} = \frac{\gamma}{\nu_t}\tau_{ij}\frac{\partial u_i}{\partial x_j} - \beta\rho\omega^2 + \frac{\partial}{\partial x_j}\left[(\mu + \sigma_\omega \mu_t)\frac{\partial \omega}{\partial x_j}\right] + 2(1 - F_1)\frac{\rho\sigma_{\omega 2}}{\omega}\frac{\partial k}{\partial x_j}\frac{\partial \omega}{\partial x_j} \tag{7}$$

where $\nu_t = \frac{\rho a_1 k}{\max(a_1\omega, \Omega F_2)}$ is the eddy viscosity; Ω is the vorticity; F_1 is the hydrodynamic function transiting k-ω model in the near wall to the k-ε model in outside the cylinder surface, which is defined as followed:

$$\phi = F_1\phi_1 + (1 - F_1)\phi_2 \tag{8}$$

$$F_1 = \tanh\left(\arg_1^4\right) \tag{9}$$

$$\arg_1 = \min\left[\max\left(\frac{\sqrt{k}}{\beta^*\omega d}, \frac{500\nu}{d^2\omega}, \frac{4\rho\sigma_{\omega 2}k}{CD_{k\omega}d^2}\right)\right] \tag{10}$$

$$CD_{k\omega} = \max\left(2\rho\sigma_{\omega 2}\frac{1}{\omega}\frac{\partial k}{\partial x_j}\frac{\partial \omega}{\partial x_j}, 10^{-20}\right) \tag{11}$$

$$F_2 = \tanh\left(\arg_2^2\right) \tag{12}$$

$$\arg_2 = \max\left(2\frac{\sqrt{k}}{\beta^*\omega d}, \frac{500\nu}{d^2\omega}\right) \tag{13}$$

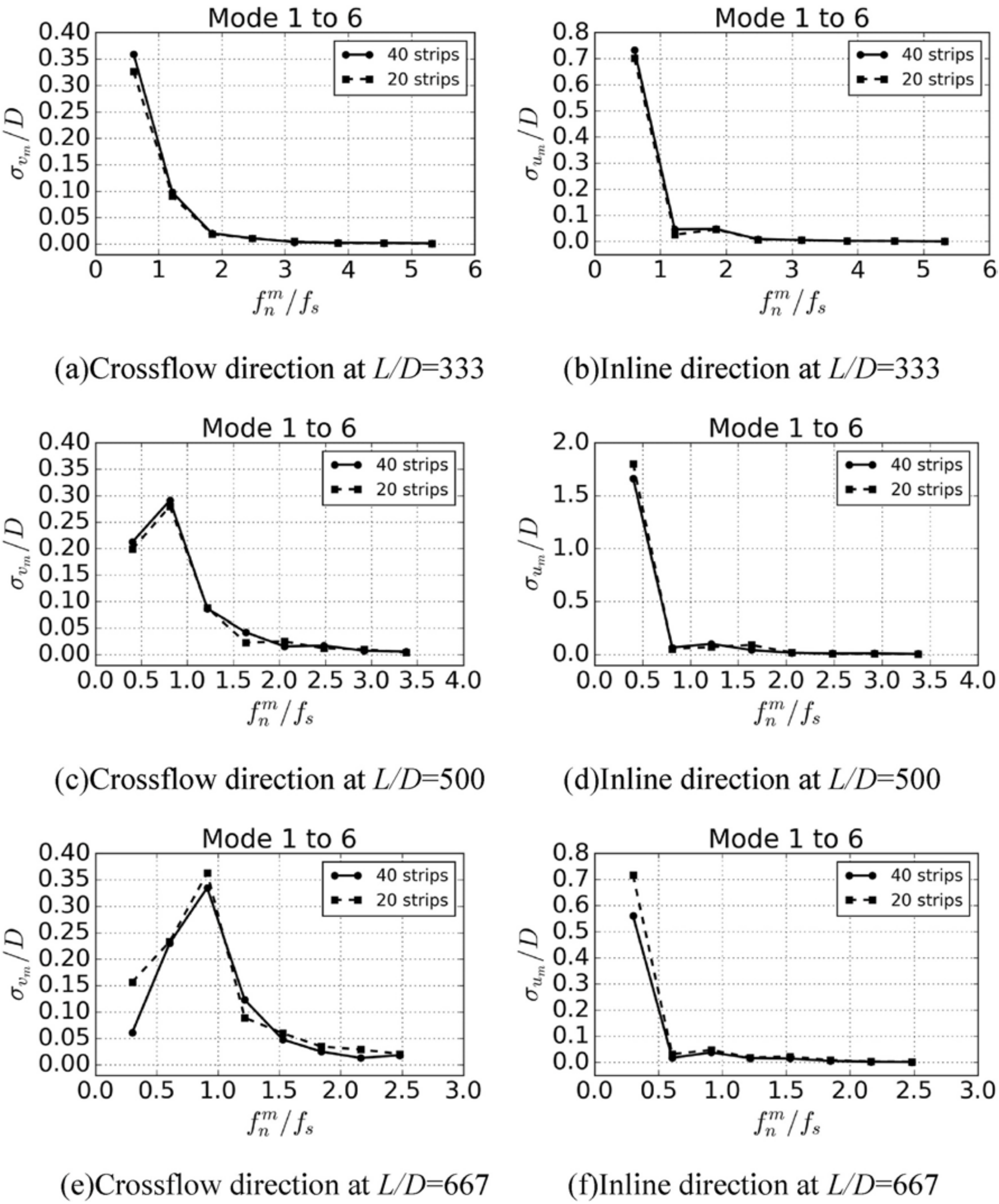

Fig. 9. Comparison of non-dimensional vibration modal weights STD of the cylinder between 20 and 40 fluid strips of different aspect ratios in both directions.

where $\beta^* = 0.09$; $\sigma_{k1}, \sigma_{\omega1}, \beta_1, a_1, \gamma_1$ are the empirical coefficients in the *k*-*ω* model and $\sigma_{k2}, \sigma_{\omega2}, \beta_2, \gamma_2$ are the empirical coefficients in the *k*-*ε* model.

2.4. Structural governing equations

For a flexible cylinder with large aspect ratio, it can be considered as a flexural elastic structure satisfying the Bernoulli–Euler bending beam hypothesis. Thus, the cylinder vibrations are calculated through this model and the FEM method in this paper. The support excitation method that has been verified available in solving structural vibrations of a flexible cylinder with large scale motions by Fu et al. (2018) is used in present study. The inline displacement (*x* direction) can be written as the sum of the support frame motion and the relative inline vibration of the cylinder shown as Eq (14):

$$x_{total}(z,t) = x_{frame}(t) + x(z,t) \tag{14}$$

where $x_{total}(z,t)$ is the total inline displacement of all nodes along the cylinder; $x_{frame}(t)$ is the support frame displacement at both ends; $x(z,t)$ is the relative inline vibration displacement.

The equilibrium of force components in the system can be expressed as Eq (15):

$$f_{hydro} = f_{inertial} + f_{damping} + f_{spring} \tag{15}$$

where f_{hydro} is the hydrodynamic force acted on the cylinder; $f_{inertial}$ is the inertial force calculated through the kinetic energy of the cylinder;

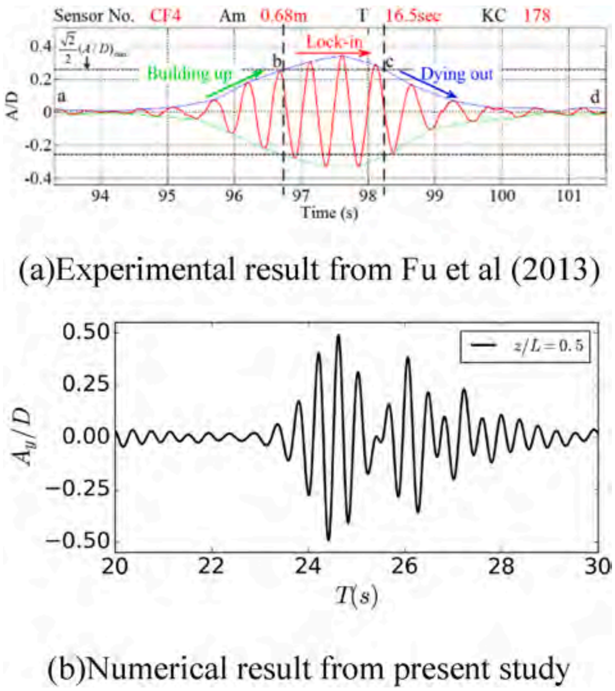

Fig. 10. Comparison of the VIV developing process in the half oscillating period at the mid-span cylinder.

$f_{damping}$ is the damping force calculated through the damping and the vibration velocity of the cylinder; f_{spring} is the spring force calculated through the stiffness and the vibration displacement of the cylinder. Then the Mass-Spring-Damping (MCK) equations of the system in both directions can be written as Eq (16) and Eq (17):

$$m\ddot{x} + c\dot{x} + kx = f_{hydrox} - m\ddot{x}_{frame} \tag{16}$$

$$m\ddot{y} + c\dot{y} + ky = f_{hydroy} \tag{17}$$

where m, c, k are the mass, the damping and the stiffness of the system; f_{hydrox}, f_{hydroy} are the inline and the crossflow hydrodynamic forces respectively. Through the FEM method, the governing equations of the system can be expressed as Eq (18) and Eq (19):

$$M\left\{\ddot{X}\right\} + C\left\{\dot{X}\right\} + K\{X\} = \{F_{\mathrm{HX}}\} - M\left\{\ddot{X}_{\mathrm{frame}}\right\} \tag{18}$$

$$M\left\{\ddot{Y}\right\} + C\left\{\dot{Y}\right\} + K\{Y\} = \{F_{\mathrm{HY}}\} \tag{19}$$

where M, C, K are the mass, damping and stiffness matrixes of the system; $\{\ddot{X}_{\mathrm{frame}}\}$ is the acceleration vector of the support frame in the in-line direction; $\{F_{\mathrm{HX}}\}, \{F_{\mathrm{HY}}\}$ are hydrodynamic force vectors in both directions. The Rayleigh Damping is used to generate the damping matrix as shown in Eq (20) and Eq (21) based on the first two natural frequencies of the cylinder listed in Table 1.

$$C = \alpha M + \beta K \tag{20}$$

$$\begin{bmatrix} \alpha \\ \beta \end{bmatrix} = \frac{2\varsigma}{f_{n1} + f_{n2}} \begin{bmatrix} 2\pi f_{n1} f_{n2} \\ ^{1}/_{(2\pi)} \end{bmatrix} \tag{21}$$

where α and β are proportionality coefficient; ς is the damping ratio; f_{n1} and f_{n2} are the first two natural frequencies of the cylinder.

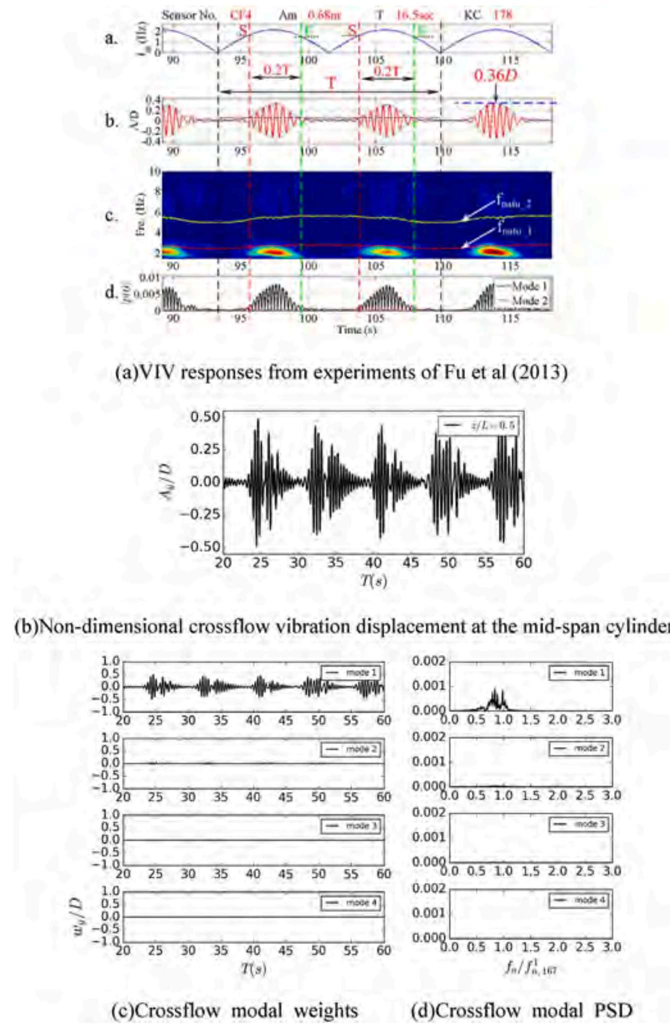

Fig. 11. Comparisons of VIV responses between experiment and present simulation.

3. Validation studies

3.1. Numerical model setup

The 2D strip theory requires calculating hydrodynamic forces in multiple 2D fluid planes located at intervals along the cylinder span. Therefore, a suitable choice of the fluid strip number and the mesh resolution is benefit for the well capture of the highest vibration mode and the prediction of hydrodynamic forces. Through researches of Willden and Graham (2001, 2004), they found that a minimum of three fluid strips were required per vibration mode for correct capture on the axial variation of the phasing of the hydrodynamic forces with respect to the cylinder vibration. During their simulations, 64 fluid strips were used with the maximum vibration mode reached around the 10th mode.

Considering the dominant vibration mode in the experiment of Fu et al. (2013) kept the 1st mode at $KC = 178$, 20 fluid strips are sufficient to capture the 1st mode in the validation study. The layout of the computational model is shown in Fig. 3. All strips share the same computational domain and mesh distribution. Velocity inlet condition is specified at the inlet boundary and pressure outlet condition is applied in the outlet boundary. Wall condition is specified at the cylinder surface boundary, while symmetry conditions are for the top and bottom boundaries. On account of the Finite Volume Method used in the OpenFOAM, the 3D computational grid is required during the flow field calculation. Therefore, the “empty” condition, which represents the

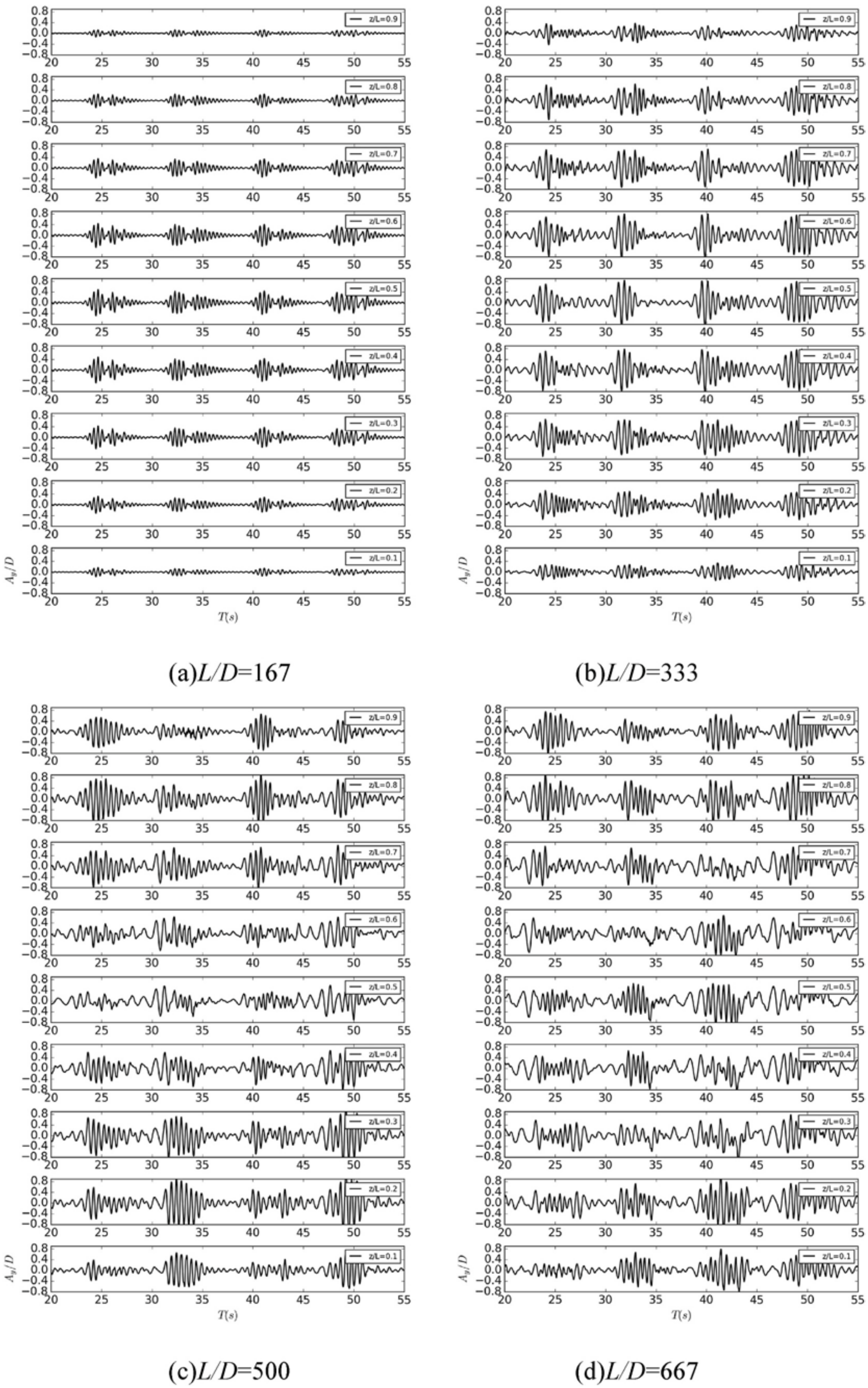

Fig. 12. Comparison of non-dimensional crossflow vibration displacement along the cylinder in multi oscillating periods.

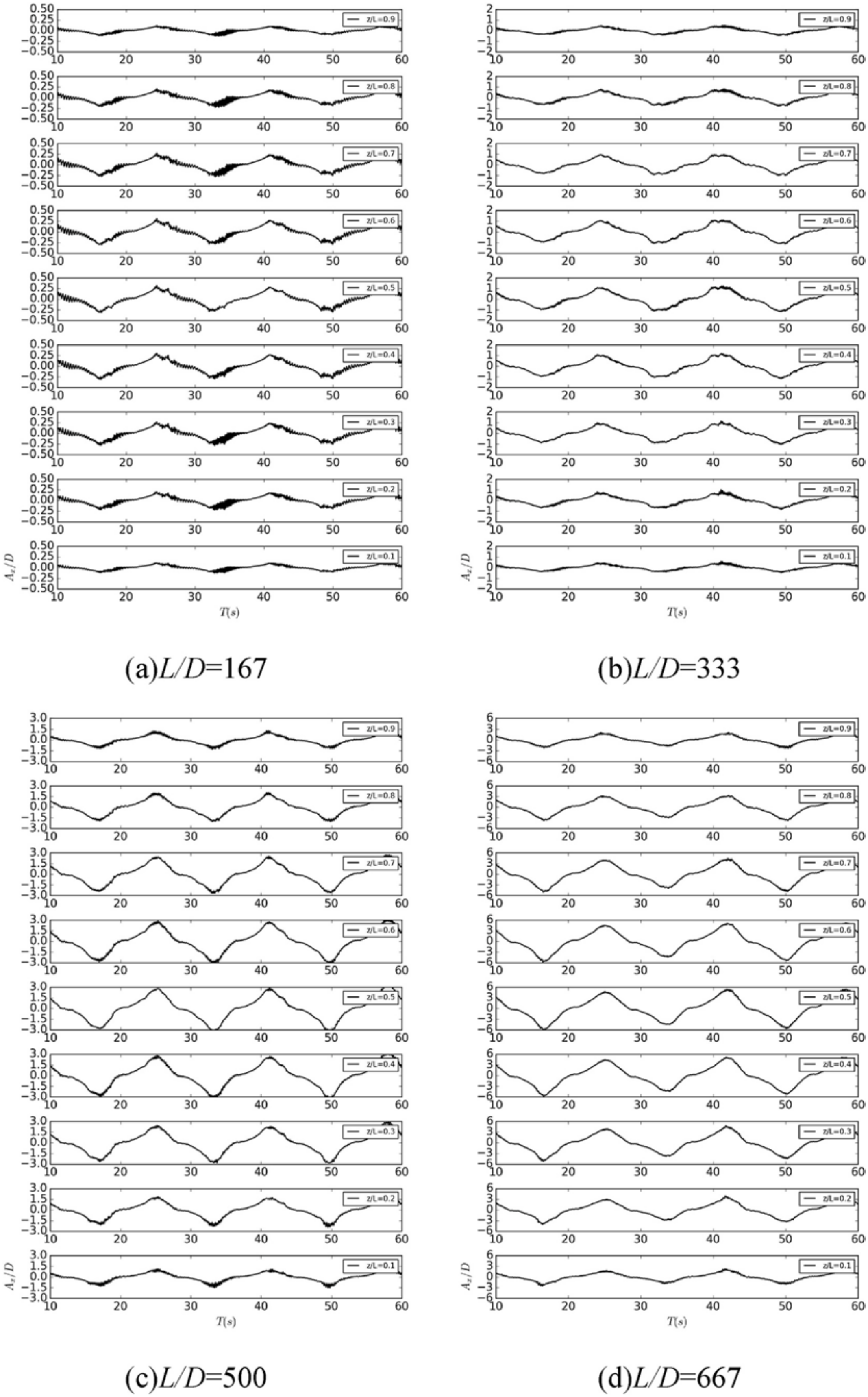

Fig. 13. Comparison of non-dimensional inline vibration displacement along the cylinder in multi oscillating periods among different aspect ratios.

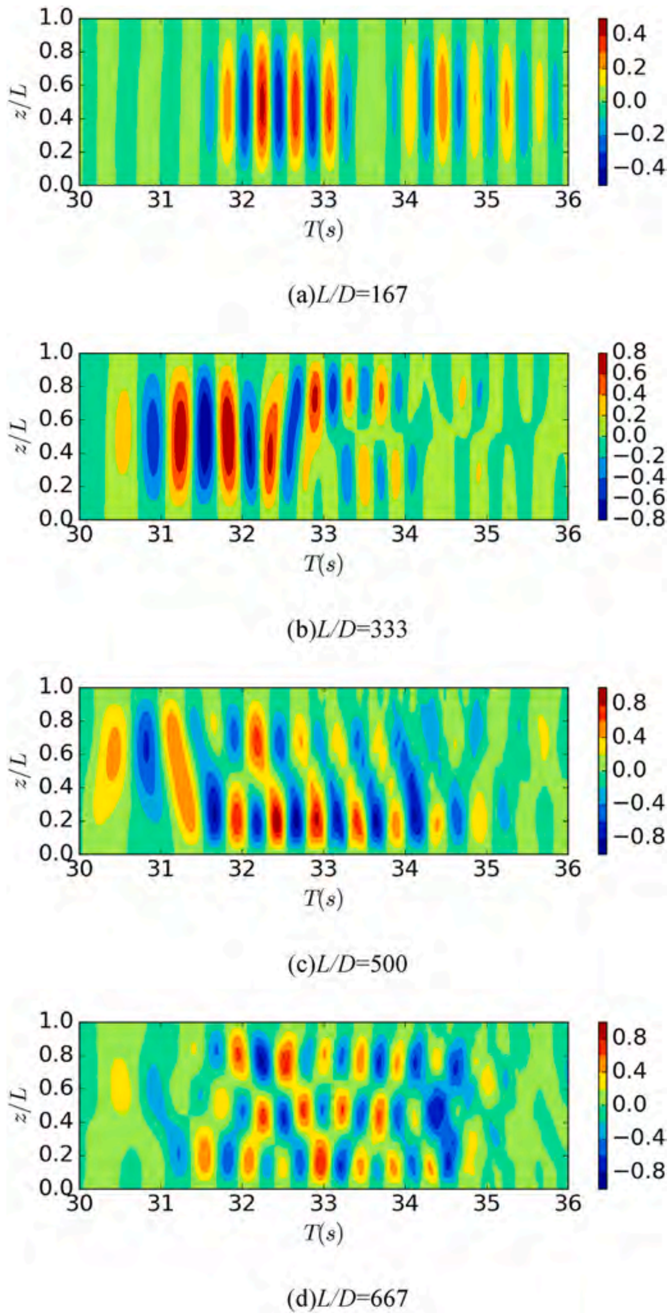

Fig. 14. Comparison of non-dimensional crossflow spatio-temporal vibration displacement among different aspect ratios.

neglect of numerical simulation in the axial direction (z direction), specified at the front and back boundaries realizes the generation of the 2D computational grid as shown in Fig. 4 (a).

The dynamic mesh technique is used to update the computational mesh at every time step. Since the KC number is set to be 178 in all simulations, the oscillating amplitude of support frames in the inline direction is extremely large compared with the crossflow vibration amplitude. In order to guarantee the mesh quality during simulations, each fluid strip is 180D in the inline direction and 40D in the crossflow direction. Mesh near the cylinder surface is refined and the $y+$ keeps around 2.0 in all simulations to predict turbulence kinetic energy in the boundary layer as shown in Fig. 4 (b). The updated mesh is shown in Fig. 4 (c) and (d) when support frames oscillate to its leftmost position. It can be found that the computational mesh of the left part has been compressed while the right part has been stretched obviously. However, the mesh around the cylinder surface almost keeps the same as that at the initial condition in the circular domain, which guarantees the mesh quality and minimizes the effect of mesh deformation during the hydrodynamic forces calculation. The flexible cylinder is discretized into 80 structural elements with 81 nodes in total. The time step is set as 0.0002s to ensure the Courant Number lower than 2.0 during the implicit solution process, which guarantees the stability and the convergence rate in all simulations.

In order to analyze the vibration frequency features, the modal analysis method that has been testified to be valid by Chaplin et al. (2005) and Fu et al. (2018) is adopted. Thus, displacements in the crossflow and the inline directions can be expressed as the sum of a series of modal shapes as followed:

$$\phi_m(z) = \sin\left(\frac{m\pi}{L}z\right) \tag{22}$$

$$x(z,t) = \sum_{m=1}^{N} u_m(t)\cdot\phi_m(z) \tag{23}$$

$$y(z,t) = \sum_{m=1}^{N} v_m(t)\cdot\phi_m(z) \tag{24}$$

where z is the axial location of the structural nodes; L is the cylinder length; $m = 1, 2, 3$ and etc; $x(z,t)$ is the relative inline displacement of all nodes along the cylinder; $y(z,t)$ is the crossflow displacement of all nodes; $u_m(t)$ is the time-dependent modal weight vector of the mth mode in the inline direction; $v_m(t)$ is the time-dependent modal weight vector of the mth mode in the crossflow direction and N is the mode number. Then, figures of modal decomposition and power spectral density (PSD) of each modal weight normalized by the cylinder diameter D are obtained.

3.2. Mesh convergence study

Computational mesh convergence study is conducted among three meshes with 0.45 million, 0.8 million and 1.4 million cells to verify the mesh dependence. Magnitudes of the crossflow and inline vibration responses are provided by the standard deviations (STD) with respect to time of the STD of $y(z,t)$ and $x(z,t)$ over z as expressed in Eq(25) and (26). STD of modal weights σ_{y^m} and σ_{u^m} are defined in the same way. The natural frequencies f_n^m (the mth order of the natural frequency) of the cylinder are normalized by the Strouhal frequency as shown in Eq (27).

$$\sigma_y = \sqrt{\frac{1}{T}\int_0^T \frac{1}{L}\int_0^L y(z,t)^2 dzdt} \tag{25}$$

$$\sigma_x = \sqrt{\frac{1}{T}\int_0^T \frac{1}{L}\int_0^L [x(z,t) - \bar{x}(z)]^2 dzdt} \tag{26}$$

$$f_s = \frac{U_m \cdot St}{D} \tag{27}$$

where $\bar{x}(z)$is the time-averaged inline displacement, T is the time interval for data processing, $St = 0.2$ is the Strouhal number used in present analysis.

Fig. 5 shows comparison of vibration displacements STD along the cylinder in both directions, which presents the 1st modal shape among different mesh resolutions. Relatively obvious computational errors can be observed between the coarse mesh and the medium mesh of the maximum crossflow displacement STD and its corresponding axial location. Meanwhile, good agreement is obtained among three meshes in the inline direction. Fig. 6 shows comparison of non-dimensional vibration modal weights STD versus non-dimensional natural frequencies among three mesh resolutions. The peak vibration mode in each fold line represents the dominant vibration mode of the cylinder.

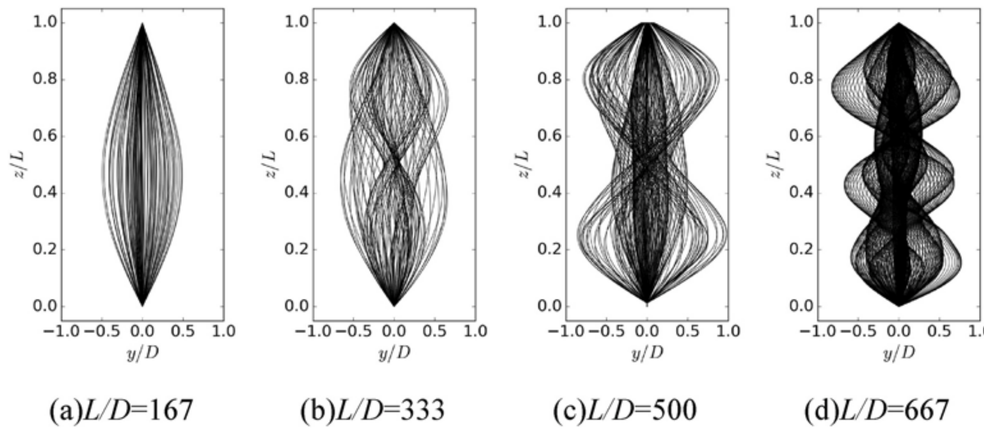

Fig. 15. Comparison of crossflow vibration deflections among different aspect ratios.

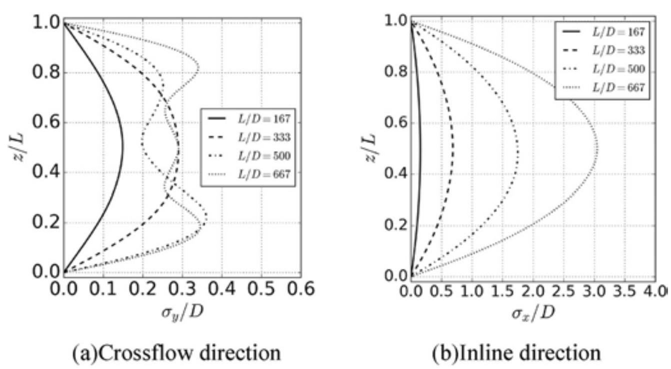

Fig. 16. Comparison of non-dimensional vibration displacement STD of the cylinder among different aspect ratios in both directions.

The cylinder shows the 1st vibration mode where the corresponding non-dimensional frequency is around 1 in both directions, indicating the occurrence of the resonance phenomenon. Effects of other vibration modes are too small to be considered. It can be known that the dominant vibration mode and the corresponding modal weight amplitude agree well between the medium mesh and the fine mesh, while computational errors exist between the medium mesh and the coarse mesh in both directions. Therefore, the medium mesh with 0.8 million cells is employed for further investigations based on the mesh resolution convergence study.

3.3. Fluid strips convergence study

The fluid strips convergence study among 10 strips, 20 strips and 40 strips respectively is carried out at $L/D = 167$. Fig. 7 and Fig. 8 are comparisons of STD of vibration displacements and modal weights in both directions. From these figures, it can be found that good agreement of the maximum vibration displacement STD and its corresponding axial location can be obtained between the 20 fluid strips simulation and the 40 fluid strips simulation in both directions. Comparatively large computation error is observed from 10 fluid strips simulation in the crossflow direction where both the maximum vibration displacement STD and its axial location are overestimated. The 1st dominant vibration mode is correctly captured in both directions among three simulations from modal weights STD. Variation tendency from the 2nd vibration mode to the 6th vibration mode shows high degree of similarity with the same magnitude.

Meanwhile, comparisons on VIV responses of a flexible cylinder with larger aspect ratio between 20 fluid strips and 40 fluid strips at the same conditions are also conducted. Fig. 9 shows corresponding modal weights STD in both directions. It can be found that the variation tendency shows high similarity especially at $L/D = 333$ and 500 in both directions. Although comparatively large computational errors appear at the 1st vibration mode in both directions when the aspect ratio reaches 667, dominant vibration modes are correctly captured with the same magnitude using different number of fluid strips. It can be concluded that 20 fluid strips can capture main vibration characteristics well with comparatively fewer computational meshes and computational time in present study.

3.4. Numerical validation study

Comparison of the VIV developing process in half an oscillating period between previous experiment and present simulation is presented in Fig. 10. To analyze VIV responses in the half oscillatory flow, three specific regions of “Building up”, “Lock-in” and “Dying out” are defined based on the boundary value of $\frac{\sqrt{2}A_m}{2D}$ by Fu et al. (2013). The definition of the special “Lock-in” region in the VIV developing process represents the drastic VIV with comparatively large vibration displacement in each half period, which is different from the normal concept of the resonance phenomenon where the vortex shedding frequency closes to the natural frequency of the cylinder. The “Lock-in” region is 17.3% of the half oscillating period in the present simulation from Fig. 10 (b), which agrees well with the experiment result of 17% from Fig. 10 (a) of Fu et al. (2013). The maximum non-dimensional crossflow vibration amplitude in present simulation is larger than the experiment, which may result from the simplification of the practical damping replaced by the Rayleigh damping.

Comparisons of more vibration responses are shown in Fig. 11. Fig. 11 (a) shows VIV responses from experiments of Fu et al. (2013). It can be found that the specific intermittent VIV feature is observed during multiple oscillating periods. The dominant vibration mode presents the 1st vibration mode and the dominant vibration frequency is around 2.1Hz. And effects of the 2nd vibration mode to VIV responses are extremely weak in contrast to the 1st vibration mode. Fig.11 (b) to Fig.11 (d) are simulation results of the non-dimensional time-dependent crossflow displacement at the mid-span cylinder, non-dimensional time-dependent modal weights and the corresponding modal PSD respectively. Fig. 11 (b) also presents the same intermittent VIV phenomenon as the experiment with the maximum vibration amplitude shows a bit larger than that of experiment. The dominant vibration mode of the cylinder shows the 1st vibration mode from the modal weight comparison in Fig. 11 (c). Values of the 2nd, the 3rd and the 4th modal weights are extremely smaller than that of the 1st vibration mode, which is also familiar with experiment results in Fig. 11 (a). The vibration frequency region in multiple oscillating periods varies from around 1.9Hz–2.7Hz showing in Fig. 11 (d), which is in good agreement with the frequency

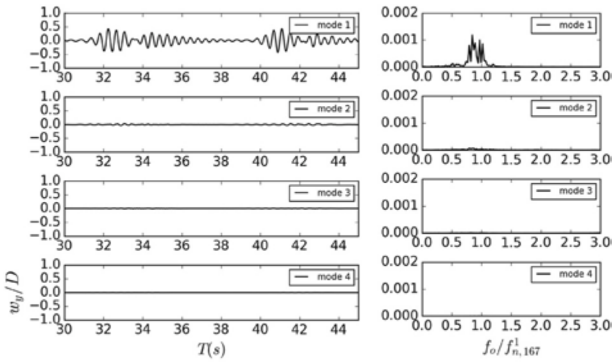

(a)L/D=167

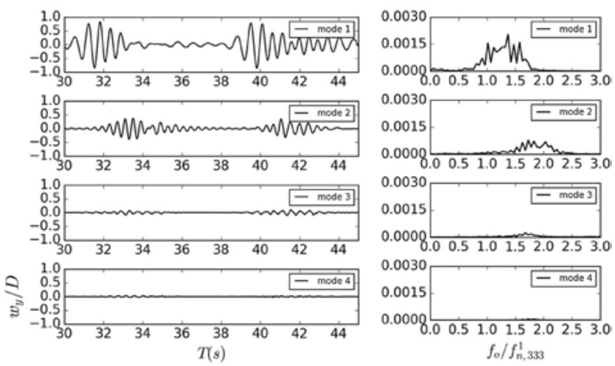

(b)L/D=333

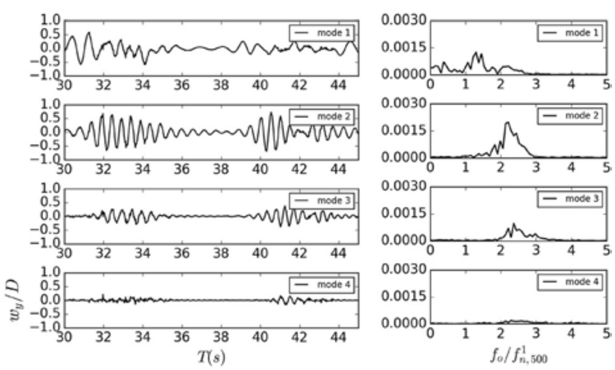

(c)L/D=500

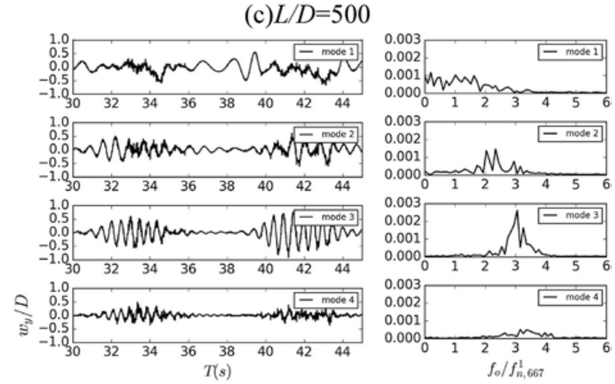

(d)L/D=667

Fig. 17. Comparison of non-dimensional crossflow vibration modal weights and corresponding modal PSD among different aspect ratios in an oscillating period.

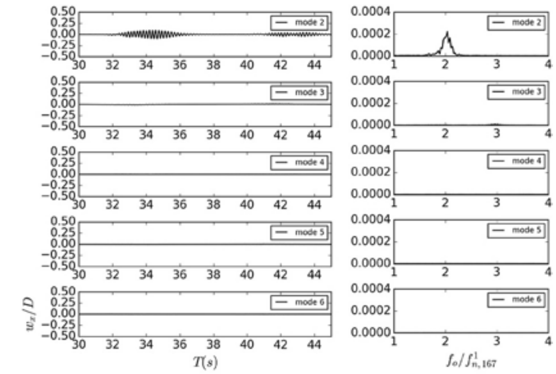

(a)L/D=167

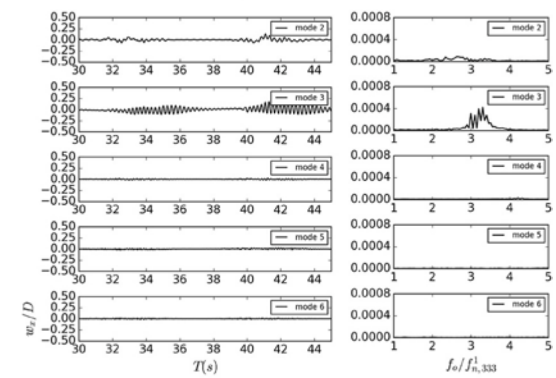

(b)L/D=333

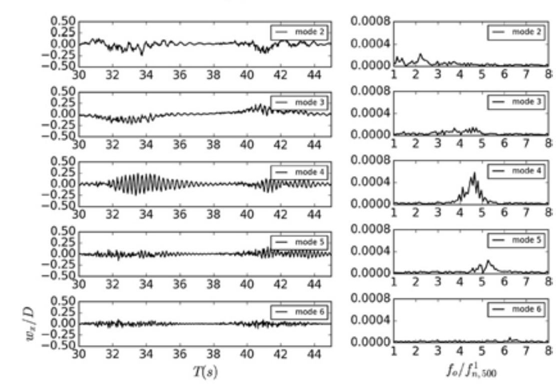

(c)L/D=500

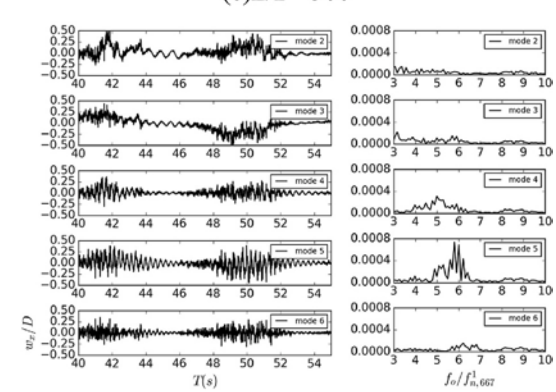

(d)L/D=667

Fig. 18. Comparison of non-dimensional inline vibration modal weights and corresponding modal PSD among different aspect ratios in an oscillating period.

Table 2
Natural frequencies of the cylinder with different aspect ratios.

Aspect ratio	$f^1_{n,L/D}$	$f^2_{n,L/D}$	Unit
167	2.68	5.46	*Hz*
333	1.31	2.63	*Hz*
500	0.872	1.75	*Hz*
667	0.654	1.31	*Hz*

analysis result in the third subplot from Fig. 11 (a). The dominant vibration frequency corresponding to the 1st dominant vibration mode is around 2.0Hz in present simulation from the peak value in Fig. 11 (d), which closes to the experiment result of 2.1Hz from Fu et al. (2013). From these comparisons, it can be known that simulation results are in good agreement with experiment results and the validity of the solver is verified.

4. Results and discussions

4.1. Time-domain vibration responses

Comparisons of nodal vibration responses from numerical simulations of a flexible cylinder with different aspect ratios in an oscillatory flow are analyzed detailedly in this section. Almost all parameters of these numerical models keep the same as the fundamental simulation, except that the cylinder axial length varies from 8 to 16 with an interval of 4. It means that cylinder aspect ratios are 167, 333, 500 and 667 respectively in the following analysis.

Fig. 12 presents non-dimensional crossflow vibration displacements at 9 locations along the cylinder in multiple oscillating periods. Vibration displacement of support frames gets to zero when t=(i+0 or 0.5)T (i = 0, 1, 2, etc, T = 16.5s) as presented in Eq (1), while the corresponding relative oscillatory flow velocity gets its maximum value. While the relative velocity will approach zero when vibration displacement of support frames gets to its peaks and valleys at t=(i+0.25)T and (i+0.75)T respectively. The specific "Lock-in" region, defined by Fu et al. (2013), occurs at around $t = 2.5T$ and $3.0T$ in Fig. 12 (a) when the frame velocity gets its maximum value. The maximum vibration amplitude at the mid-span cylinder is around 0.5D in the "Lock-in" region when $L/D = 167$, while it decreases to around 0.1D at locations of $z/L = 0.1$ and 0.9. The vibration amplitude shows the same magnitude in "Building up" and "Dying out" regions where VIV responses are comparatively weaker than that in the "Lock-in" region.

When the cylinder aspect ratio increases to 333, the maximum non-dimensional crossflow vibration amplitude increases to around 0.8 around the mid-span cylinder as shown in Fig. 13(b). The vibration amplitude at $z/L = 0.1$ and 0.9 increases to around 0.3D, which is three times of that at $L/D = 167$. The vibration amplitude variation among all locations along the cylinder at $L/D = 333$ shows similar tendency as that at $L/D = 167$.

The maximum non-dimensional crossflow vibration amplitude at locations of $z/L = 0.2$ and 0.8 increases to around 0.8 in the "Lock-in" region when the cylinder aspect ratio reaches 500 as shown in Fig. 12 (c). Meanwhile, the maximum vibration amplitude at the mid-span cylinder decreases to around 0.5D. The vibration amplitude variation tendency at $L/D = 500$ is opposite to that at $L/D = 167$ and 333. No apparent increase of the vibration amplitude appears in "Building up" and "Dying out" regions due to the weak VIV responses of the cylinder in these regions where the oscillating velocities are close to zero. The non-dimensional crossflow vibration amplitude is around 0.8 at nodes of z/L

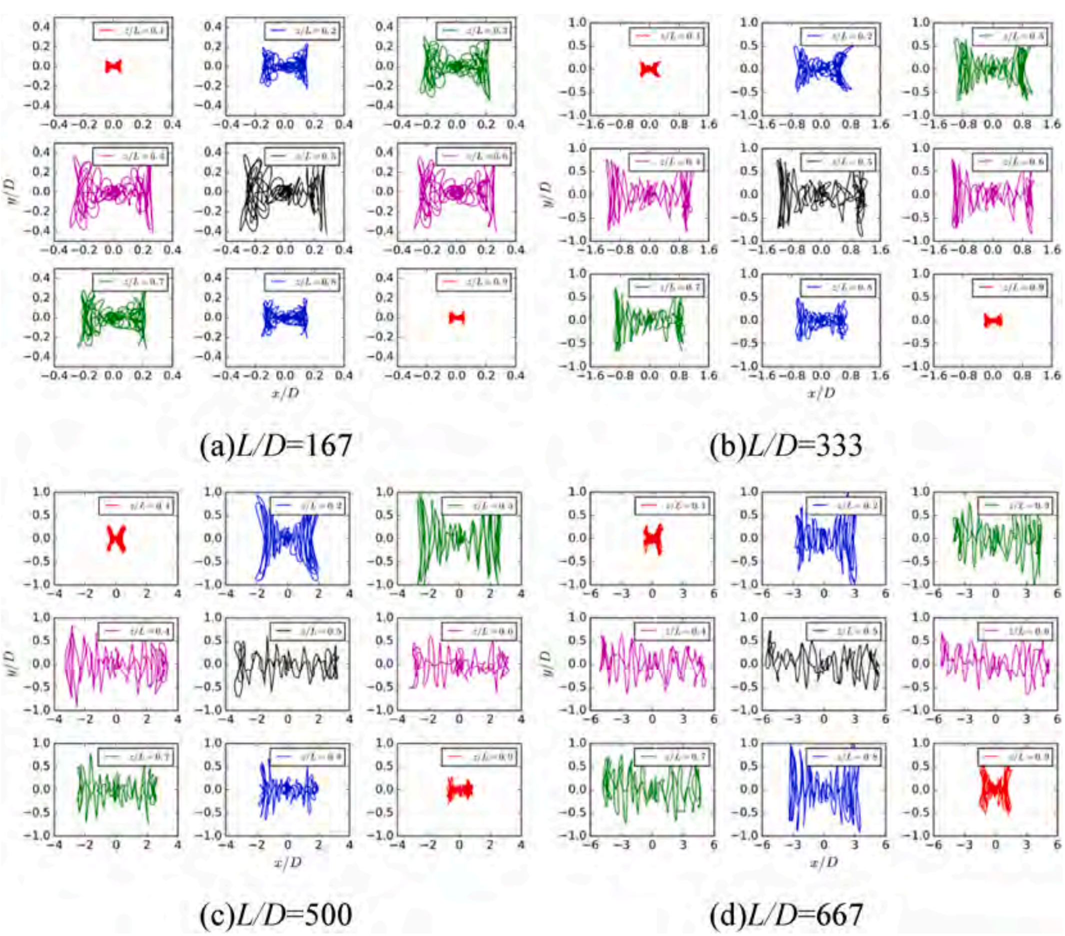

Fig. 19. Comparison of non-dimensional vibration trajectories along the cylinder among different aspect ratios.

= 0.2 and 0.8 when the cylinder aspect ratio reaches 667, while the vibration amplitude increases to around 0.7D at the mid-span cylinder compared with that at L/D = 500. It can be found that the specific intermittent VIV developing process varies obviously with the increase of the cylinder aspect ratio, compared between Fig. 12(a) and (d).

Non-dimensional inline displacements along the cylinder span in multiple oscillating periods are presented in Fig. 13. The maximum relative non-dimensional inline vibration amplitude increases from around 0.25 to 5.0 with the increase of the cylinder aspect ratio. Since the oscillation of support frames shows a sinusoidal function shape as expressed in Eq (1), the relative oscillatory flow U_w can be written as followed:

$$U_w(t) = -U_m \cdot \cos\left(\frac{2\pi}{T}t\right) \tag{28}$$

It is obvious that the relative oscillatory flow velocity and the relative inline displacement are synchronous. It can be found in Fig. 13(a) that the maximum relative non-dimensional inline vibration displacement around its inline equilibrium position gets to its maximum value at t= (i+0 or 0.5)T (i = 0, 1, 2, etc), where the support frames move across the original position and the corresponding oscillating velocity gets to its maximum. The vibration amplitude gets its maximum value at the mid-span cylinder during all simulations, which is very different from the crossflow variation tendency at high aspect ratios compared between Figs. 13(d) and Fig.12(d) where the dominant inline vibration mode keeps the 1st mode and the dominant crossflow vibration mode increase to the 2nd and 3rd modes. A high frequency vibration phenomenon is observed at the rightmost or the leftmost positions during the oscillation of support frames. The source of the special phenomenon may result from the reattachment effects of existing vortices shed during the previous half oscillating period, which has been detailed explained in simulation of Fu et al. (2018). When the cylinder aspect ratio gets larger, this high vibration frequency phenomenon turns to happen mainly in the "lock-in" region. Another significant finding is that an inflection point is observed at t=(0.25 or 0.75 + i)T (i = 0, 1, 2, etc) in "Building up" and "Dying out" regions when support frames approach its rightmost or leftmost positions.

Non-dimensional crossflow spatio-temporal displacements and typical vibration deflections along the cylinder are shown in Fig. 14 and Fig. 15 where the red-to-blue color bar represents the magnitude of the crossflow vibration displacement. Crossflow vibration of all nodes is in-phase from the spatio-temporal displacement along the cylinder in Fig. 14 (a). It can be known that the cylinder presents the 1st dominant vibration mode, which corresponds to the typical crossflow vibration deflection in Fig. 15 (a). Crossflow vibrations of upper and nether nodes transfers from in-phase vibration to anti-phase vibration when the cylinder aspect ratio increases to 333, which contributes to the vibration shape transition phenomenon from the 1st mode shape to the 2nd mode shape around the "Lock-in" region as shown in Figs. 14 (b) and Fig.15 (b). The travelling wave phenomenon along the cylinder span can be observed between two standing wave phenomena. The 1st modal standing wave occurred in the "Lock-in" region with larger vibration amplitude than that of the 2nd modal standing wave, which can be observed through the gradation of the red or blue color.

Combining Fig. 12 (c) with Figs. 14 (c) and Fig.15 (c), the vibration shape transition phenomenon of the "1st modal standing wave – travelling wave – 2nd modal standing wave" developing process is also observed. The main difference between L/D = 333 and L/D = 500 is that the 2nd vibration shape is occurred and becomes the dominant vibration shape in the "Lock-in" region. The 1st vibration shape mainly occurs in "Building up" and "Dying out" regions. The variation on the dominant vibration shape corresponds to the variation shown in Fig. 12 at L/D = 500. The vibration deflection increases to the 2nd and the 3rd mode shapes when L/D = 667. The 3rd modal standing wave is observed in the "Lock-in" region and the 2nd modal standing wave is observed in "Building up" and "Dying out" regions, while the vibration shape transition phenomenon occurs between them.

The vibration deflection changes from single mode to multi-modes under the effect of the cylinder aspect ratio. The dominant vibration deflection increases from the 1st vibration shape to the 3rd vibration shape in the "Lock-in" region with the cylinder aspect ratio increases as shown in Fig. 15. The vibration shape transition phenomenon of the "standing wave – travelling wave – standing wave" developing process can be observed clearly when the cylinder aspect ratio is larger than 333 as shown in Figs. 14 and 15. The travelling wave phenomenon can only be observed during each VIV developing process when the VIV regions change from the "Building-up" region to the "Lock-in" region or from the "Lock-in" region to the "Dying-out" region where the relative oscillatory flow velocity changes obviously as shown in Fig. 14(b), (c) and (d).

Comparison of displacements STD along the cylinder in both directions present in Fig. 16. It can be found that the maximum non-dimensional displacement STD increases from 0.15 at the mid-span cylinder to 0.35 at z/L = 0.2 and 0.8, which are in good agreement with the crossflow vibration variation tendency in Fig. 12. The vibration shape along the cylinder span increases from the 1st mode shape to the 3rd mode shape when L/D increases from 167 to 667. The maximum non-dimensional inline displacement STD increases from 0.2 to 3.05 as shown in Fig. 16 (b) with the increase of the cylinder aspect ratio. However, the vibration deflection keeps the 1st mode shape in all simulations, which corresponds with the sinusoidal shape of the time dependent inline vibration displacements as shown in Fig. 13. It represents that the 1st mode plays remarkable controlling effect to the inline vibration responses of the cylinder.

4.2. Modal and frequency-domain responses

Comparison of modal weights and corresponding modal PSD of the cylinder in the crossflow and inline directions are presented in Fig. 17 and Fig. 18 respectively. The modal PSD is normalized by the 1st natural frequency $f^1_{n,L/D}$ of the cylinder. The first two order natural frequencies of the cylinder among different aspect ratios are shown in Table .2.

It can be found that the dominant vibration mode of the cylinder at L/D = 167 is apparently the 1st vibration mode from Fig. 17 (a). Effects of higher vibration modes are too small to be considered. Multi-frequency components are observed in the modal PSD. Variation on the oscillating velocity leads to the variation of the Re number and vortex shedding features in each half oscillating period. Two frequency peaks in the modal PSD of Fig. 17 (a) correspond to vibration frequencies in each "Lock-in" region during the VIV developing process in an oscillating period. Lower frequency components in the modal PSD represent corresponding vibration frequencies in "Building up" and "Dying out" regions. When L/D = 333 as shown in Fig. 17 (b), the dominant vibration mode keeps the 1st vibration mode as L/D = 167. The dominant vibration frequency in the "lock-in" region is around $1.4f^1_{n,L/D=333}$. Although, effects of the 2nd vibration mode become obvious at L/D = 333, it is still covered by the 1st vibration mode during most time. The dominant vibration mode will turn to the 2nd vibration mode only when the modal weight amplitude of the 2nd vibration mode exceeds the 1st vibration mode during the VIV developing process, such as at the time region from T = 33s to T = 35s as shown in the time-dependent modal weights in Fig. 17(b). Therefore, the mode transition phenomenon can hardly be observed.

However, this phenomenon becomes more obvious when L/D = 500. The dominant vibration mode increases to the 2nd vibration mode with the corresponding dominant vibration frequency reaches around $2.2f^1_{n,L/D=500}$. Obvious modal weights of the 3rd and the 4th vibration modes, whose effects to VIV responses are totally covered by the 2nd vibration mode, are also observed in Fig. 17 (c). Multi-dominant vibration modes phenomenon is generated when the aspect ratio increases to 667 as shown in Fig. 17 (d). Since modal weight magnitudes of the

2nd and the 3rd vibration modes are very similar in the "Lock-in" region, the dominant vibration mode will shift between these modes and vibration features will become more complicated. Corresponding dominant vibration frequencies are around $2.4f^1_{n,L/D=667}$ and $3.0f^1_{n,L/D=667}$respectively. It can be concluded that the dominant crossflow vibration mode will increase and the multi-mode vibration phenomenon will appear with the increase of the cylinder aspect ratio. Although the non-dimensional frequencies present a decrease tendency with the increase of the cylinder aspect ratio, the actual dominant vibration frequencies still keep around 2.0Hz due to the decrease of the natural frequencies.

The time-dependent relative inline vibration shape of all nodes performs similar sinusoidal function shape as shown in Fig. 13, which contributes to the dominant 1st vibration mode in all simulations. Effects of higher vibration modes are totally covered due to the extremely large modal weight of the 1st vibration mode. In order to analyze modal vibration characteristics in the inline direction, the controlling effect of the 1st vibration mode on modal weights and corresponding modal PSD is removed as presented in Fig. 18. The high order of vibration mode increases from the 2nd vibration mode to the 5th vibration mode at an interval of 1 with the increase of the cylinder aspect ratio. The corresponding vibration frequency at $L/D = 167$ is around $2.0f^1_{n,L/D=167}$and it increases to around $3.3f^1_{n,L/D=333}$, $4.6f^1_{n,L/D=500}$and $5.8f^1_{n,L/D=667}$respectively when the cylinder aspect ratio increases from 333 to 667. High order vibration frequencies in the inline direction are around twice of dominant vibration frequencies in the crossflow direction at the same aspect ratio compared between Figs. 17 and 18. Although more high order vibration modes are excited, almost only one dominant vibration mode appears when removing the 1st dominant vibration mode in the inline direction. Observing from the time-dependent modal weights, it can also be found that multi-modes vibration phenomenon appears when the aspect ratio increase to 500 as shown in Fig. 18(c), which is similar to the phenomenon that observed in the crossflow direction as shown in Fig. 17.

4.3. Vibration trajectories

In order to illustrate the relationship between the crossflow and the inline vibrations more directly, vibration trajectories at 9 axial locations from $z/L = 0.1$ to 0.9 along the cylinder in an oscillating period are presented in Fig. 19. The obvious butterfly type of vibration trajectory can be observed at all locations when $L/D = 167$ and the butterfly shape at the mid-span cylinder is larger than that at other locations, which corresponds to the variation tendency of vibration displacements in Figs. 12 and 13. Two sides of the butterfly trajectory are generated in the "Lock-in" region where crossflow and inline vibration amplitudes approach its maximum values at the same time. The vibration amplitude decreases apparently in both directions when the vibration locates in "Building up" and "Dying out" regions, which contributes to the generation of the middle part of the butterfly vibration trajectory.

When the aspect ratio reaches 333, the increase rate of the vibration amplitude in the inline direction is larger than that in the crossflow direction, which leads to the comparatively large enlargement of the butterfly type of vibration trajectory in the inline direction as shown in Fig. 19 (b). Meanwhile, vibration shapes at all nodes keep the butterfly type due to the dominant 1st vibration modes in both directions. Since the dominant vibration mode transfers to the 2nd vibration mode in the crossflow direction and keeps the 1st vibration mode in the inline direction in the "Lock-in" region at $L/D = 500$, the butterfly type of vibration trajectory changes to the stripe type, especially at the mid-span cylinder as shown in Fig. 19 (c). The butterfly shape can still be observed at upper and nether nodes along the cylinder, which is similar to that in Fig. 19 (b). The slenderness of the strip type of vibration trajectory increases when the cylinder aspect ratio increases to 667. The butterfly type of vibration trajectory gradually disappears on account of the appearance of the 3rd vibration mode in the "Lock-in" region. From comparisons of vibration trajectories, it can be found that the vibration trajectory shape turns from the butterfly type to the stripe type with the increase of the cylinder aspect ratio. However, axial locations near both ends of the cylinder hardly be affected and keep the butterfly type of vibration trajectory.

5. Conclusions

A series of numerical investigations on VIV of a flexible cylinder in an oscillatory flow with different aspect ratios have been conducted in this paper using the viv-FOAM-SJTU solver. The fundamental simulation is based on experiments of Fu et al. (2013) at $KC = 178$. Simulation results have been compared and analyzed detailedly. The specific "Building up – Lock-in – Dying out" VIV developing process is also observed in present study. In order to exclude disturbances from the mesh resolution and the number of fluid strips, computational mesh and fluid strips convergence studies have been carried out. The medium mesh with 0.8 million cells and 20 fluid strips has been chosen for subsequent simulations. In the crossflow direction, the dominant vibration mode increases from the 1st vibration mode to the 3rd vibration mode with the increase of the cylinder aspect ratio. The maximum vibration amplitude increases remarkably when the aspect ratio increase from 167 to 500. The vibration amplitude decreases to around 0.7D and the multi-modes vibration phenomenon appears when the aspect ratio reaches 667. In the inline direction, the dominant vibration mode keeps the 1st vibration mode and the maximum vibration amplitude keeps increasing from around 0.25D to 5.0D. The normalized dominant vibration frequency varies from 0.75 $f^1_{n,L/D=167}$to $3.0f^1_{n,L/D=667}$in the crossflow direction and from $2.0f^1_{n,L/D=167}$ to $5.8f^1_{n,L/D=667}$in the inline direction. As for the vibration trajectory, it changes from the butterfly shape to the slender stripe shape when the cylinder aspect ratio increases. While it keeps the butterfly shape at locations near both ends of the cylinder in all simulations.

Author statement

Di Deng: Data curation, Writing-Original draft preparation, Visualization, Investigation, Software, Validation. Weiwen Zhao: Software, Data curation, Visualization, Investigation, Validation. Decheng Wan (Corresponding author): Supervision, Conceptualization, Methodology, Investigation, Writing-Reviewing and Editing.

Declaration of competing interest

The authors declare the following financial interests/personal relationships which may be considered as potential competing interests:

Decheng Wan reports financial support was provided by Shanghai Jiao Tong University.

Acknowledgments

This work is supported by National Natural Science Foundation of China (51879159), the National Key Research and Development Program of China (2019YFB1704200 and 2019YFC0312400), to which the authors are most grateful.

References

Bearman, P.W., 1989. A visual study of the flow around an oscillating circular cylinder at low Keulegan-Carpenter numbers and low Stokes numbers[J]. J. Fluid Mech. 211 (157), 157–182.

Chaplin, J.R., Bearman, P.W., Huera Huarte, F.J., et al., 2005. Laboratory measurements of vortex-induced vibrations of a vertical tension riser in a stepped current[J]. J. Fluid Struct. 21 (1 SPEC. ISS.), 3–24.

Chen, W.M., Fu, Y.Q., Guo, S.X., et al., 2016. Fluid-solid coupling and hydrodynamic response of vortex-induced vibration of slender ocean cylinders[J]. Advances in Mechanics 38 (5), 604.
Duan, M.Y., Wan, D.C., Xue, H.X., 2016. Prediction of Response for Vortex-Induced Vibrations of a Flexible Riser Pipe by Using Multi-Strip method[C] Proceedings of the Twenty-Sixth (2016) International Ocean and Polar Engineering Conference Rhodes, Greece, June 26-July 1, pp. 1065–1073.
Duan, M.Y., Fu, B.W., Wan, D.C., 2016b. The Effect of Top Tension on VIV Model Analysis of a Vertical Flexible Riser[C] Proceedings of the Second Conference of Global Chinese Scholars on Hydrodynamics, Nov. 11-14, pp. 455–460. Wuxi, China.
Duan, M.Y., Zou, L., Wan, D.C., 2017. Numerical simulations of vortex-induced vibrations of a flexible riser with different aspect ratios in uniform and shear currents [J]. Journal of Hydrodynamics, Ser. B 29 (6), 1010–1022.
Duan, M.Y., Zou, L., Wan, D.C., 2018. Numerical analysis of multi-modal vibrations of a vertical riser in step currents[J]. Ocean Engineering 152, 428–442.
Fonias, E.N., Grigoriadis, D.G.E., 2018. Large Eddy Simulation of near-bed pipelines in oscillatory flow[J]. Coastal Engineering 133, 76–91.
Fu, S.X., Wang, J.G., Baarholm, R., et al., 2013. VIV of Flexible Cylinder in Oscillatory Flow. In: International conference on offshore mechanics and arctic engineering, OMAE, june 9–14, 2013, Nantes, France, OMAE2013-10348.
Fu, B.W., Zou, L., Wan, D.C., 2018. Numerical study of vortex-induced vibrations of a flexible cylinder in an oscillatory flow[J]. J. Fluid Struct. 77, 170–181.
Huang, X.D., Zhang, H., Wang, X.S., 2009. An overview on the study of vortex-induced vibration of marine riser[J]. Journal of Marine Sciences 27 (4), 95–101.
Ji, C.N., Li, F.F., Chen, W.L., et al., 2015. Progress and prospect of the study on vortex-induced vibration of circular cylinders[J]. J. Ocean Technol. 34 (1).
Kozakiewicz, A., Sumer, B.M., Fredsøe, J., et al., 1997. Vortex regimes around a freely vibrating cylinder in oscillatory flow[C]. Int. J. Offshore Polar Eng. 7 (2), 94–103.
Lie, H., Kaasen, K.E., 2006. Modal analysis of measurements from a large-scale VIV model test of a riser in linearly sheared flow[J]. J. Fluid Struct. 22 (4), 557–575.
Meneghini, J.R., Saltara, F., Fregonesi, R.D.A., et al., 2004. Numerical simulations of VIV on long flexible cylinders immersed in complex flow fields[J]. Eur. J. Mech. B Fluid 23 (1), 51–63.
Menter, F.R., 1993. Zonal Two Equation K-ω Turbulence Models for Aerodynamic flows [R]. AIAA-93-2906.
Munir, A., Zhao, M., Wu, H., et al., 2018. Numerical investigation of the effect of plane boundary on two-degree-of-freedom of vortex-induced vibration of a circular cylinder in oscillatory flow[J]. Ocean Engineering 148, 17–32.
Nehari, D., Armenio, V., Ballio, F., 2004. Three-dimensional analysis of the unidirectional oscillatory flow around a circular cylinder at low Keulegan–Carpenter and β numbers[J]. J. Fluid Mech. 520, 157–186.
Pearcey, T., Zhao, M., Xiang, Y., et al., 2017. Vibration of two elastically mounted cylinders of different diameters in oscillatory flow[J]. Appl. Ocean Res. 69, 173–190.
Ren, H.J., Xu, Y.W., Cheng, J.Y., et al., 2019. Vortex-induced vibration of flexible pipe fitted with helical strakes in oscillatory flow[J]. Ocean Engineering 189 (May), 106274.
Sarpkaya, T., 2004. A critical review of the intrinsic nature of VIV[J]. Fluid Mech. Appl. 75, 159–161.
Sarpkaya, T., 1986. Force on a circular cylinder in viscous oscillatory flow at low Keulegan-Carpenter numbers[J]. J. Fluid Mech. 165, 61–71.
Scandura, P., Armenio, V., Foti, E., 2009. Numerical investigation of the oscillatory flow around a circular cylinder close to a wall at moderate Keulegan-Carpenter and low Reynolds numbers[J]. J. Fluid Mech. 627, 259–290.
Sumer, B.M., Fredsøe, J., 1988. Transverse vibrations of an elastically mounted cylinder exposed to an oscillating flow[J]. J. Offshore Mech. Arctic Eng. 110, 387–394.
Sun, L., Zong, Z., Dong, J., et al., 2012. Stripwise discrete vortex method for VIV analysis of flexible risers[J]. J. Fluid Struct. 35, 21–49.
Thorsen, M.J., Sævik, S., Larsen, C.M., 2016. Time domain simulation of vortex-induced vibrations in stationary and oscillating flows[J]. J. Fluid Struct. 61, 1–19.
Tong, F., Cheng, L., Zhao, M., et al., 2015. Oscillatory flow regimes around four cylinders in a square arrangement under small and conditions[J]. J. Fluid Mech. 769, 298–336.
Wan, D.C., Duan, M.Y., 2017. A recent review of numerical studies on vortex-induced vibrations of long slender flexible risers in deep sea[J]. Chin. Q. Mech. 38 (2), 179–196.
Wang, J.H., Zhao, W.W., Wan, D.C., 2019. Development of naoe-FOAM-SJTU solver based on OpenFOAM for marine hydrodynamics[J]. J. Hydrodyn. 31 (1), 1–20.
Wang, J.G., Fu, S.X., Xu, Y., et al., 2014. VIV developing process of a flexible cylinder under oscillatory flow[J]. Chin. J. Theor. Appl. Mech. 46, 173–182.
Wang, J.G., Fu, S.X., Baarholm, R., et al., 2015. Fatigue damage induced by vortex-induced vibrations in oscillatory flow[J]. Mar. Struct. 40, 73–91.
Willden, R.H.J., Graham, J.M.R., 2001. Numerical prediction of VIV on long flexible circular cylinders[J]. J. Fluid Struct. 15 (3–4), 659–669.
Willden, R.H.J., Graham, J.M.R., 2004. Multi-modal Vortex-Induced Vibrations of a vertical riser pipe subject to a uniform current profile[J]. Eur. J. Mech. B Fluid 23 (1), 209–218.
Williamson, C.H.K., 1985. Sinusoidal flow relative to circular cylinders[J]. J. Fluid Mech. 155, 141–174.
Williamson, C.H.K., Govardhan-Ankulkar, R., 2004. Vortex-induced vibrations[J]. Annu. Rev. Fluid Mech. 36, 413–455.
Xu, W., Ã, X.Z., Wu, Y., 2008. High aspect ratio (L/D) riser VIV prediction using wake oscillator model[J]. Ocean Engineering 35, 1769–1774.
Yamamoto, C.T., Meneghini, J.R., Saltara, F., et al., 2004. Numerical simulations of vortex-induced vibration on flexible cylinders[J]. J. Fluid Struct. 19 (4), 467–489.
Yuan, Y.C., Xue, H.X., Tang, W.Y., 2018. Numerical analysis of Vortex-Induced Vibration for flexible risers under steady and oscillatory flows[J]. Ocean Engineering 148, 548–562.
Zhao, M., Cheng, L., An, H.W., 2012. Numerical investigation of vortex-induced vibration of a circular cylinder in transverse direction in oscillatory flow[J]. Ocean Engineering 41, 39–52.
Zhao, M., 2013. Numerical investigation of two-degree-of-freedom vortex-induced vibration of a circular cylinder in oscillatory flow[J]. J. Fluid Struct. 39, 41–59.
Zhao, M., Kaja, K., Xiang, Y., et al., 2013. Vortex-induced vibration (VIV) of a circular cylinder in combined steady and oscillatory flow[J]. Ocean Engineering 73, 83–95.
Zhao, M., Cheng, L., 2014. Two-dimensional numerical study of vortex shedding regimes of oscillatory flow past two circular cylinders in side-by-side and tandem arrangements at low Reynolds numbers[J]. J. Fluid Mech. 751, 1–37.